



Automatic initialization of active contours and level set method in ultrasound images of breast abnormalities

Annupan Rodtook^a, Khwunta Kirimasthong^b, Wanrudee Lohitvisate^c,
Stanislav S. Makhanov^{d,*}

^a Department of Computer Science, Ramkhamhaeng University, Thailand

^b School of Information Technology, Mae Fa Luang University, Thailand

^c Department of Radiology, Thammasat University, Thailand

^d School of Information and Computer Technology, Sirindhorn International Institute of Technology, Thammasat University, Thailand



ARTICLE INFO

Article history:

Received 18 October 2016

Revised 1 September 2017

Accepted 28 January 2018

Available online 2 February 2018

Keywords:

Ultrasound image segmentation

ABSTRACT

We propose a novel initialization method designed for active contours (AC) and the level set method (LSM), based on walking particles. The algorithm defines the seeds at converging and diverging configurations of the corresponding vector field. Next, the seeds “explode”, generating a set of walking particles designed to differentiate between the seeds located inside and outside the object. The exploding seeds method (ESM) has been tested against five state-of-the-art initialization methods on 180 ultrasound images from a database collected by Thammasat University Hospital of Thailand. The set of images was additionally partitioned into malignant tumors, fibroadenomas and cysts. The method has been tested for each of those cases using the ground truth hand-drawn by leading radiologists of the hospital. The competing methods were: the trial snake (TS), centers of divergence (CoD), force field segmentation (FFS), Poisson Inverse Gradient Vector Flow (PIG), and quasi-automated initialization (QAI). The numerical tests demonstrated that CoD and FFS failed on the selected test images, whereas the average accuracy of PIG and QAI were lower than that achieved by the proposed method for both AC and the LSM. The LSM combined with the ESM provides the best results.

© 2018 Elsevier Ltd. All rights reserved.

1. Introduction

Since the seminal work [1] AC (snakes) have been applied to many segmentation problems derived from different applications. Further improvements are gradient vector flow (GVF) [2] and the generalized gradient vector flow field (GGVF) [3]. Some variations of these ideas are multidirectional GGVF [4] and the non-linear diffusion model [5]. Recent modifications of the GVF-type model are Normal Gradient Vector Flow [6], Infinity Laplacian [7], Harmonic Gradient Vector Flow [8], Convolution Vector Flow [9], Dynamic Directional Gradient Vector Flow [10], Adaptive Diffusion Flow [11], and Multi Feature Gradient Vector Flow [12]. A comparative study of AC methods in medical image segmentation is presented in [61].

The accuracy and the computational time of segmentation produced by the AC depend on their initial positions (seeds). The seeds must be initialized close to the desired object. Otherwise the AC attach to false boundaries created by noise and artifacts.

One of the popular solutions is analysis of the vector field generated by the GVF-type model. Since the noise and small artifacts generate star-like (divergent or convergent) configurations of the vector field, multiple AC generated around them avoid the false boundaries. For instance, [13] applies force field segmentation (FFS) to divide the image domain into disjointed regions representing the capture range of the external force field. The AC are individually initialized within each of the enclosures and moved to the targeted object boundary within it, avoiding being attracted by other objects. However, the algorithm transforms the image segmentation problem into a vector field segmentation problem, which is difficult to solve if strong noise is present.

The idea to initialize the snakes at the centers of divergence/convergence (CoD) of the corresponding vector field was proposed in [14]. Ge and Tan [15] introduce the CoD by computing relative directions of the vector field in a 2×2 window. He et al. [16] uses phase portrait analysis (PPA) [17] to find critical points of the vector field. Although PPA has been used in a variety of image processing applications, e.g. [17–22], neither [15] nor [16] differentiate the external and internal snakes. Therefore, the image produced by [15] requires a special merging procedure to re-

* Corresponding author.

E-mail address: makhanov@siit.tu.ac.th (S.S. Makhanov).

move boundaries due to over segmentation. Further, [16] uses only seeds characterized by a certain gray level associated with the object. Therefore, the method fails on low contrast images characterized by shadows and artifacts such as the ultrasound (US) images of breast abnormalities.

The importance of the critical points was noticed in [23]. The authors propose to merge multi-snakes initialized around those points for segmentation of the MRI images of lungs. However, the method works only when the snakes are initialized inside the lungs.

A competing idea is placing the seed points uniformly or randomly over the entire image, evolving the snakes from each seed point and analyzing the resulting configuration. For instance, [24] runs ACs until their convergence to a local minima and constructs a pattern image (an annular band around each snake). Next, the algorithm projects each pattern image into an already trained principal component classifier. The snakes associated with a lower reconstruction error are classified as objects and others as non-objects. However, the required classifier to validate the final configuration must be trained. Classification of randomly initialized snakes is computationally expensive and may lead to considerable inaccuracies. The final configurations, which depend on the relative speed of the snakes' evolution, can differ considerably.

Another interesting approach is the quasi-automated initialization (QAI) method by Tauber et al [25,26]. The method employs CoDs, combined with a tracing procedure to create a "skeleton" of the object, consisting of centers of strong and weak divergence. The centers of weak divergence are the points where the vectors of the GVF diverge in one (either horizontal or vertical) direction. The centers of strong divergence feature both horizontal and vertical divergences. The initial snake is generated around the skeleton. However, the initialization is not entirely automatic. The algorithm still requires at least one manually generated point inside the object. Moreover, in noisy images, the skeleton evolves outside the boundary of the object even though the manually generated point is correct.

Poisson Inverse Gradient Vector Flow (PIG) [27] establishes a relationship between the external force field and the underlying external energy field via the solution of the corresponding Poisson equation. The isoline of the minimum energy is selected as the initial contour. The model has been applied to 2D and 3D cases for a variety of medical images. However, the method may suffer from incomplete isolines, as well as from over segmentation.

An automatic initialization method has been proposed in [28] for PET images of the liver. The candidate contours are generated by Canny edge detection and subsequently classified by a genetic algorithm. The algorithm has been applied to segmentation of face contours in video files [29]. A similar idea was introduced in [30] for detection of the synovial boundaries in US images. However, the proposed initial snakes selected from the edge map are not robust and may not be applicable to multiple objects.

The initialization algorithms for the US images often rely on gray levels and textures to place the seed points inside the tumor [31–33]. Saliency and feature maps have been proposed in [34]. Fergani et al. [35] introduces a special vector field to hybridize the GVF and the texture. A Chan–Vese type model is proposed in [36]. A few papers related to a specific medical image processing task use the typical position of a human organ in the US images (see, for instance, [37]). However, these models are image dependent and may not work if strong noise is present.

Trial snakes (TS) method, combined with PPA, was applied to US images of breast cancer in [38]. The PPA makes it possible to detect the centers of convergence and divergence, as well as attracting and repelling nodes. The algorithm differentiates between the internal and external seeds by running multiple TS from the critical points and checking their intersections with the boundary

of the image. The most serious drawback of TS is that it requires a considerable amount of computational time.

In 1988, Osher and Sethian proposed the level set method (LSM) [44,57], in which the contour curve is implicitly represented as the zero level set of a high dimensional function (also called the level set function). The method is a strong competitor of AC since it can automatically handle topological changes of multiple contours. The contours can merge, split and collapse in a natural and efficient way, which is not allowed in parametric AC [45].

The existing LSMs are categorized into edge-based [44–47] and region-based versions [48–52]. The region based models often produce poor segmentation results due to a wrong movement of the evolving contour when the image is characterized by a heterogeneous intensity. This model is "very sensitive to initialization and easily gets stuck into local minima" [53,54], which is a major problem for complex medical images.

Through stop functions, edge-based LSMs use the gradient information to attach the contour curve to the object boundary. Since the gradient is used as the stopping criteria, edge-based LSMs segment images without any limitations on the homogeneity of the objects of interest. A classical example of an edge based LSM is the geodesic AC model proposed by Caselles et al. [45]. Distance regularized level set evolution (DRLSE) proposed by Li et al. [46,47] is one of the most popular edge-based LSMs. The method eliminates the need for re-initialization of the contour required by the preceding methods, and thereby avoids its induced numerical errors.

All of the above initialization methods can be applied, to obtain the initial contour for the LSM close to the genuine boundary of the object, or initialize multiple initial contours.

Therefore, we have developed a new initialization method suitable for both: AC and LSM. We compare it with preceding methods in terms of efficiency and accuracy.

2. Methodology

The new fast algorithm for automatic initialization combines a new force field analysis based on circular projection (CP), multiple initial contours and walking particles generated by the exploding seeds.

The main steps of the ESM algorithm are given below.

1. Preprocessing (a standard procedure such as Gaussian filtering).
2. Evaluation of the gradient vector field.
3. Detection of the converging/diverging configuration (stars) using CP.
4. Merging closely located stars into a single region.
5. Initializing walking particles generated by seeds at the star-like configurations.
6. Selecting seeds located inside the object and initializing the initial contours.
7. Segmentation by AC or LSM.

It should be noted that the idea of using walking particles for *edge detection* has been proposed in [39]. However, their use for *initialization* has been overlooked. Besides, [39] employs "charged" particles which *attach themselves* to the edges. As opposed to that, our proposed particles *bounce off* the edges. This creates a totally different model suitable for fast initialization. Therefore, the main contribution of this paper is a new exploding seed method (ESM) to automatically initialize AC and the initial surface for the LSM in the US images of breast cancer.

The ESM has been tested against five state-of-the-art models mentioned above, namely, TS [38], FFS [13], CoD [15,16], QAI [25,26], and PIG [27]. With regard to the above methods, the ESM provides faster and more accurate initializations, which leads to more accurate segmentations. The proposed algorithm has been

combined with a recent modification of AC called the Adaptive Diffusion Flow (ADF) snakes [11] and the recent distance regularized level set method (DRLSE) [46,47] for a set US images of breast abnormalities (benign and malignant). The above methods were selected as the most prominent representatives of the AC and LSM families. Finally, we compare AC and the LSM. The LSM with the walking particles provides the best results.

2.1. Active contours

An active contour (snake) is a parametric curve $X(s) \equiv (x(s), y(s))$ which grows or contracts inside the image to attach itself to the boundary of the desired object. The evolution of the snake is simulated by Euler equations, corresponding to minimization of a certain energy functional [1]. The equations are given by

$$aX_{ss} + bX_{ssss} + V = 0, \quad (1)$$

where the subscripts denote partial derivatives, a and b are weighting parameters to control the snake's tension and rigidity, and $V \equiv (v_x, v_y)$, the GVF field. One of the most popular is the generalized gradient vector flow (GGVF) [3], obtained by solving the following system of partial derivative equations

$$V_t - g(|\nabla f|)\nabla^2 V - h(|\nabla f|)(\nabla f - V) = 0, \quad (2)$$

where $g(|\nabla f|) = e^{-(|\nabla f|/K)}$, $h(|\nabla f|) = 1 - g(|\nabla f|)$, $f = \nabla G_\sigma * I$, G_σ is the Gaussian kernel with the standard deviation, σ and K is a calibration parameter. Among numerous extensions of this idea are Normal Gradient Vector Flow [6], Infinity Laplacian [7], Harmonic Gradient Vector Flow [8], Convolution Vector Flow [9], Dynamic Directional Gradient Vector Flow [10], ADF snakes [11], and Multi Feature Gradient Vector Flow [12] as well as statistically based AC such as the Student's-t mixture model [56]. In this paper we use a modification of multiple ADF snakes, capable of merging, splitting, and collapsing (disappearing) when necessary.

2.2. Level set method

The contour $X(s, t)$ as the zero level set of a time dependent level set function (LSF) $\phi(x, y, t)$. Assuming that the embedding LSF takes negative values inside the zero level contour and positive values outside the Euler equation for the DRLSE energy functional is given by

$$\phi_t = \mu \operatorname{div}(d_p |\nabla \phi| \nabla \phi) + \lambda \delta_\varepsilon(\phi) \operatorname{div}(g' |\nabla \phi| / \nabla \phi) - \alpha g' \delta_\varepsilon(\phi),$$

where $g'(x, y)$ is the DRLSE edge indicator function given by

$$g' = \frac{1}{1 + |f|^2}.$$

μ, λ, α are the weighting coefficients, d_p is the double-well potential for the distance regularization [44,45] and δ_ε is a "hat" function with a variable support ε and amplitude $\frac{1}{2\varepsilon}$ [47].

DRLSE not only eliminates the need for re-initialization required by the preceding LSM routines, but also allows the use of a binary step function as the initial LSF. The region of non-zero LSF can often be obtained by a simple rough segmentation, such as thresholding. Consequently, only a small number of iterations is required to move the zero level set to the desired object boundary. The recent modifications are the Local Regional Fitting LSMs [54,55] and the hybrid models which combine the region and the edge-based fitting terms. Examples are the Dual Minimization LSM [58] and the Hybrid Diffusion LSM [59] (see also a recent survey in [60]). It is overkill to present all the different level-set methods in this short paper, therefore, in the forthcoming chapters we use DRLSE as one of the most popular representatives of the LSMs.

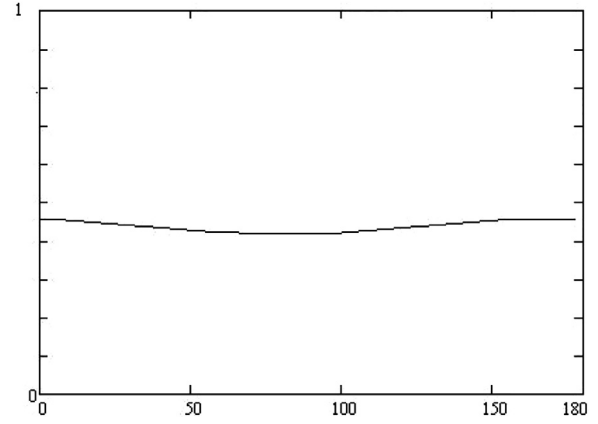


Fig. 1. Typical graph $P^+(\theta)$ ($P^-(\theta)$) for the repelling or attracting star. Note that we also apply CP at the edge detection stage (preprocessing) using the fact that $D_{i,j}$ must be large at the boundary.

2.3. Circular projection

Consider a window $W_{i,j}^k$ with size k , centered at a point i, j , on a discrete vector field $V_{i,j}$. The CP is defined by

$$P_{i,j}^+(\theta) = \sum_{i,j} \begin{cases} (\operatorname{proj}_{v_R(\theta)} V_{i,j})^2 & \text{if } \operatorname{proj}_{v_R(\theta)} V_{i,j} > 0, \\ 0, & \text{otherwise,} \end{cases}$$

and

$$P_{i,j}^-(\theta) = \sum_{i,j} \begin{cases} (\operatorname{proj}_{v_R(\theta)} V_{i,j})^2 & \text{if } \operatorname{proj}_{v_R(\theta)} V_{i,j} < 0, \\ 0, & \text{otherwise.} \end{cases}$$

where $v_R(\theta) = \begin{pmatrix} \cos \theta \\ \sin \theta \end{pmatrix}$, $0 \leq \theta \leq \pi$.

Similarly to PPA [40–42], CP reveals the "signatures" of the most important configurations which characterize the vector field. However, CP has a wider range than PPA. In particular, PPA can not detect the "boundary corner" or a chaotic vector field. Furthermore, PPA is based on linearization of the underlying vector field and includes star, saddle point, repelling/attracting node, node saddle, shear, center, and focus. Therefore, one of the above classes *must* be selected even when the field is entirely random. The configurations "center" and "focus" are practically useless since the images usually produce irrotational vector fields. As opposed to that, CP does not rely on linearization. The patterns include the "boundary corner", "chaotic" vector field (see Table 1), allowing other configurations to be defined.

We introduce a "star detector" given by

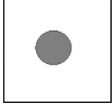
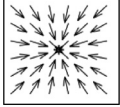
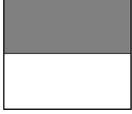
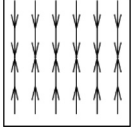
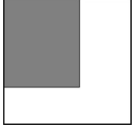
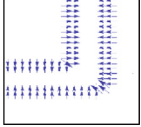

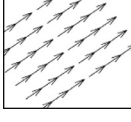
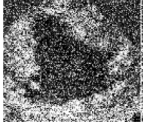

$$D_{i,j} = \max(\max_{\theta} P_{i,j}^+(\theta), \max_{\theta} P_{i,j}^-(\theta)) - \min(\min_{\theta} P_{i,j}^+(\theta), \min_{\theta} P_{i,j}^-(\theta)).$$

The detector uses the fact that the attracting and repelling stars are characterized by a small amplitude of the projections $P^+(\theta)$ and $P^-(\theta)$ (Figs. 1 and 2 illustrate the techniques).

2.4. Exploding seeds

The seeds are initialized around each repelling or attracting configuration detected by the CP. Next, the initial seeds simultaneously "explode", generating a set of N_p particles moving initially along a radial direction with regard to the center of the seed (see Fig. 3(a)). The velocity of particles is subjected to random fluctuations, which prevent them from entering into repeated (cyclic) trajectories. The key feature of the model is that the particles are

Table 1
Patterns of circular projection.

CP Pattern	Description	Image	Vector field
Repelling or attracting node	Noise (small or large groups of noisy pixels)		
Boundary	Large gradients of the edge map		
Boundary corner	Large gradients of the edge map at the corner		
Slowly varying background (shear)	Relatively uniform gradients		
Chaos	Noise with random dark and light shadows		

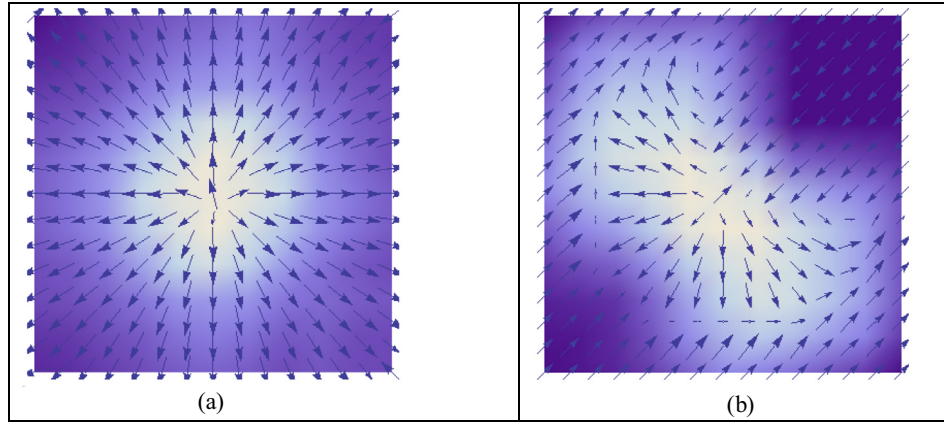


Fig. 2. CP method (a) ideal diverging configuration (light area indicates small $D_{i,j}$) (b) distorted diverging configuration (the method still works).

bouncing off the internal and external edges and disappearing (dying) at the boundary of the image. Those initialized inside the tumor stay inside, whereas particles initialized outside eventually find their way to the boundary of the image, and subsequently get deleted. Finally, since the majority of the surviving particles belong to the tumor, this separates the external and internal seeds (Fig. 3(b)). The external seeds are used to initialize the AC or LSM contours (Fig. 3(c) and (d)).

In order to avoid repeated trajectories (loops), the speed of each particle is subjected to small random perturbations (noise).

Let c_i be the center of the i -th converging/diverging star. The velocity of a particle i, j is then given by

$$v_{i,j} = \alpha v_{d,i,j} + \beta v_{r,i,j}, \quad (5)$$

where α, β are weighting parameters. The initial deterministic component of the velocity is given by $v_{d,i,j} = \begin{pmatrix} \cos \frac{2\pi j}{N_p-1} \\ \sin \frac{2\pi j}{N_p-1} \end{pmatrix}$, $j = \overline{0, N_p - 1}$.

When the particle bounces off the edge

$$v_{d,i,j,new} = -v_{d,i,j}, \quad (6)$$

The trajectory $p_{i,j}(t) \equiv \begin{pmatrix} x_{i,j}(t) \\ y_{i,j}(t) \end{pmatrix}$ of the particle i, j is given by

$$p_{i,j} = c_i + v_{i,j}t,$$

before the first collision and by

$$p_{i,j} = e_j + v_{i,j}t$$

after a collision with the edge e_j , where t denotes the pseudo-time.

As already noted, using solely v_d produces repeated (cyclic) trajectories. The random component v_r prevents the model from entering into repetitions (see Section 5 for further discussion regarding the relationship between v_d and v_r). The particles may get trapped between two or more neighboring edges. Such particles are detected, deleted, and re-initialized.

In order to ensure that the particles do not leave the object, v_j must satisfy: $|v_j| \leq \min T$, where T is the thickness of the edge.

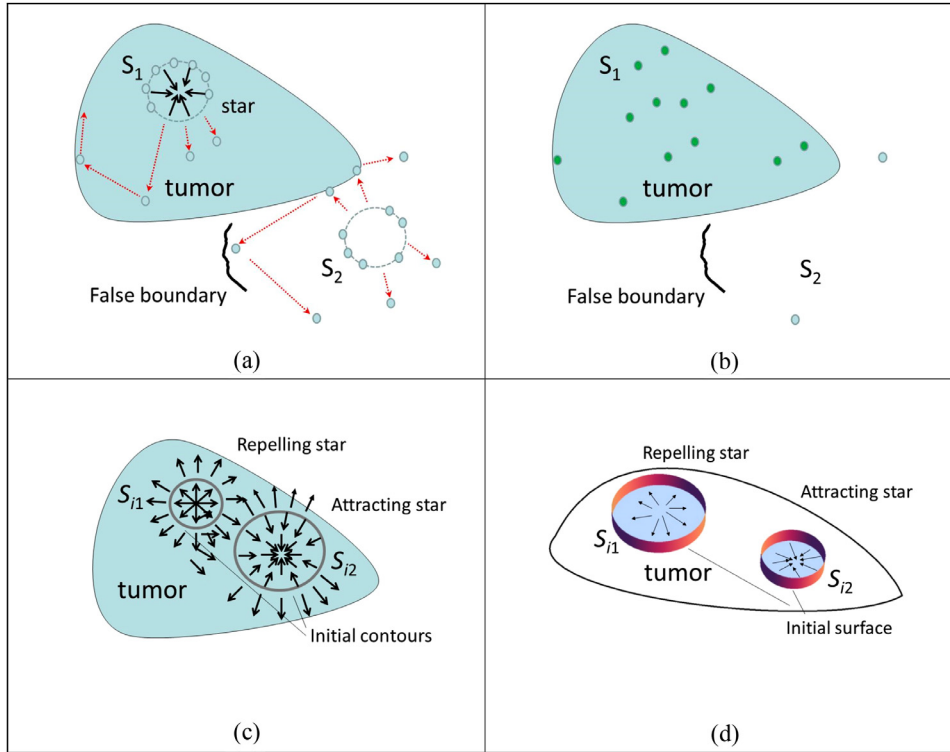


Fig. 3. Elimination of external seeds (a) seeds “explode”, (b) walking particles, (c) seeds for AC, (d) seeds for DRLSE.

Therefore, on each step, v_j is normalized, e.g. $v_{i,j,new} = \frac{Tv_{i,j}}{|v_{i,j}|}$. We do not provide a method to find T . However, if T is unknown it is safe to consider $T=1$.

If the particle reaches the boundary of the image, it is considered “dead”. The number of particles which become dead at a certain step of the algorithm is called the death rate d . The algorithm terminates when the death rate d becomes sufficiently small. We apply the following stopping criterion: $\bar{d} \leq 0.01N_{part}$, where N_{part} is the total number of particles and \bar{d} is the death rate averaged over several steps of the algorithm. The reason for using \bar{d} is that at some steps $d=0$ although the average death rate \bar{d} is still large. Further, at the first steps $d=0$ because the particles still did not reach the boundary. Therefore, this criterion applies when d reaches its maximum and starts declining (which can be easily detected).

Further, when the ESM is terminated, the seeds are classified according to the average lifetime of the corresponding seed. Denote $l_{i,j}$, the lifetime of a particle i belonging to the seed j , where $j = \overline{1, p}$ and p is the number of seeds, $i = \overline{1, N_j}$ where N_j is the number of particles belonging to the seed j . The lifetime of a particle (i, j) is the number of steps the particle stayed “alive”. The average lifetime of the seed is defined by $l_j = \frac{1}{N_j} \sum_{i=1}^{N_j} l_{i,j}$. If $l_j \leq \Delta_l$, where Δ_l denotes the corresponding threshold, the seed is classified as external, otherwise, as an internal seed.

Our forthcoming numerical experiments show that the model with appropriate control parameters separates the internal and external seeds for the US images with a 100% success rate.

The video demonstration of the method is at <http://onlinemedicalimages.com/index.php/en/presentations>

2.5. Randomizing walking particles

Recall that the velocity of a particle is given by $v_{i,j} = \alpha v_{d,i,j} + \beta v_{r,i,j}$, where α, β are weighting parameters corresponding to the

Table 2

Deterministic vs. random component of velocity.

α	S (# of iterations)	T_{comp} (computational time), sec
0.9	677	8.43
0.8	634	7.78
0.7	727	9.73
0.6	767	10.19
0.5	646	8.12

random and deterministic component of $v_{i,j}$. The parameter β ensures that the particles do not enter cyclic trajectories, so that a majority of the external particles sooner or later leave the image. On the other hand, too large β leads to abrupt trajectories and slows down the model.

Consider a normalized velocity, i.e. $v_{i,j} = \alpha v_{d,i,j} + (1-\alpha)v_{r,i,j}$, $|v_{i,j}| = 1$.

Table 2 illustrates manual tuning of the parameter α using 15 additional US images. The images were randomly selected from the database. None of the images was included in our basic test set of 180 images.

The model stops when 90% of the outside particles leave the image domain. Clearly, for this image collection, $\alpha \approx 0.8$, provides the optimal computational time.

2.6. Multiple snakes

The next stage of the algorithm employs multiple AC or LSM evolving inside the tumor. The snakes attached to the diverging stars grow and merge until they reach the boundary of the tumor. The snakes initialized around the converging stars grow, using the inverted GVF-type vector field until they stop. These snakes are re-initialized by offsetting them by several pixels to pick up the repelling component of the vector field. The snakes S_1, S_2 merge whenever $dist_{H_1}(S_1, S_2) < \delta$, where δ is the merging threshold and $dist_{H_1}$ is the Hausdorff distance (see Section 3). Some of the snakes

initialized around the repelling and attracting stars might intersect. In this case, a special tracing procedure generates a joint growing contour. For the LSM, the contours merge or collapse automatically. No additional procedures are needed.

3. Performance measures

In order to compare the ESM with the conventional algorithms we introduce the following performance measures.

3.1. Contour based accuracy measures

- The Hausdorff distance is given by $\text{dist}_{H_1}(X, Y) = \max\{\max_{a \in X} \min_{b \in Y} \|a - b\|, \max_{b \in Y} \min_{a \in X} \|a - b\|\}$, where $\| \cdot \|$ denotes the Euclidian distance, X is the ground truth contour, and Y the resulting contour.
- The averaged Hausdorff distance: dist_{H_2} obtained from dist_{H_1} by replacing the internal max by the average.
- The relative Hausdorff distance: $\text{dist}_{H_3}(X, Y) = \frac{\text{dist}_{H_1}(X, Y)}{L_X} \xi$, where L_X is the length of the true contour, and $\xi = 1000$ is the normalizing coefficient. The distance allows evaluating the relative importance of the difference between the two curves. For instance, if $\text{dist}_{H_1}(X, Y) = 10$, and $L_X = 100$ pixels, the error is unacceptable, however, if for instance, $L_X = 10,000$, then dist_{H_3} is negligible. The importance of the Hausdorff distance in comparing planar curves is that it is parametrization-invariant. Although dist_{H_1} is not a distance in a rigorous mathematical sense (it does not satisfy the triangle inequality), [43] shows that it is the best for matching the curved objects.
- The contour-based true positive rate is $TP_c = \frac{TP_Y}{N_Y}$, where TP_Y is the number of true positive pixels, and N_Y is the total number of pixels belonging to the resulting active contour.

3.2. Region based accuracy measures

- Sensitivity: $SEN = \frac{TP}{TP+FN}$.
- Specificity: $SPC = \frac{TN}{TN+FP}$.
- Accuracy: $ACC = \frac{TP+TN}{TP+TN+FP+FN}$.
- Jaccard index: $J = \frac{|X' \cap Y'|}{|X' \cup Y'|}$,

where TP , TN , FP , and FN are the region-based true positive, true negative, false positive, and false negative and where X' and Y' the set of pixels corresponding to the ground truth region and the resulting region respectively.

3.3. Performance of initialization procedure

Observe that the accuracy measures introduced in Sections 3.1 and 3.2 are only supplementary because they depend on the segmentation engine. Therefore, the performance of the initialization is evaluated by

- Percentage of images for which the internal and external seeds were correctly detected. We denote this performance indicator by N_{corr} .
- Percentage of images for which the contour was correctly segmented. The final snake is considered correct if $\text{dist}_{H_2}(X, Y) \leq \Delta_{\text{var}}$. The threshold $\Delta_{\text{var}} = 3$ was selected based on the intra-inter ground truth variation. In our experiments the ground truth contours drawn by the same expert/different experts differ as much as 3 units measured by dist_{H_2} .

As noted above, the segmentation accuracy depends not only on initialization, but on the segmentation model as well. In this paper we test closely related AC and LSM type segmentation methods.

Other methods such as clustering and region growing might benefit from the proposed ESM. However, they are out of the scope of this paper.

4. Image acquisition

The algorithm has been tested on 60 US images of breast cancer, 60 images of cysts and 60 images of fibroadenoma, from 180 different patients (see Fig. 4).

The images were obtained by a Philips iU22 ultrasound machine at Thammasat University Hospital. The ground truth contours have been hand-drawn by three leading experts with the Department of Radiology of Thammasat University using an electronic pen and a Samsung Galaxy Tablet computer. The final ground truth was obtained by the majority voting rule (two out of three). The resolution ranges from 200×200 to 300×400 pixels.

Each type of image has its own specific features, which may present some problems for segmentation routines. Malignant tumors are characterized by irregular spiculated boundary. (See Fig. 4(a) and (a')). It is well known that neither AC nor the LSM are able to accurately resolve deep concavities and sharp corners appearing at that type of the boundary. In turn, the US images of fibroadenoma are characterized by a very low contrast.

The gray levels inside the tumor are practically identical to those belonging to the shadows near the tumor. This creates the well known problem of boundary leakage [11] (See Fig. 4(b) and (b')). Finally, cyst seems to be one of the simplest objects. However, many cysts are attached to large irregular shadows, artifacts, and random noise (see Fig. 4(c) and (c')). Therefore, the procedure to generate an initial contour based on tracing (such as PIG) often selects a wrong initial boundary. Our method as well as the five competing state-of-the-art methods, namely, TS[39], FFS [13], CoD [15,16], QAI [25,26], and PIG [28], were applied without any modifications relative to the specific type of the images.

The efficiency of the initialization method is evaluated using the number of correctly initialized seeds N_{corr} (all seeds must be initialized inside the object) and the number of correctly segmented tumors S_{corr} , such that $\text{dist}_{H_2}(X, Y) \leq 3$ (see Section 3.3).

The segmentation accuracy is evaluated by three different modifications of the Hausdorff distance, H_1 , H_2 , H_3 , the contour-based true positive TP_c as well as by the region-based measures: accuracy, sensitivity, specificity, and the Jaccard index.

In order to prove the efficiency of the ESM, we apply the recent Adaptive Diffusion Flow (ADF) [11], which has been proven to be superior to GVF [2], GGVF [3], Normal Gradient Vector Flow [6], Infinity Laplacian GVF [7], Harmonic Gradient Vector Flow [8] and Convolution Vector Flow [9]. We also apply DRLSE [46,47] which has shown its superior performance with regard to the conventional methods [45].

Fig. 5 is an introductory example, comparing the initialization and the resulting contours produced by the ESM, QAI, PIG using the ADF snakes, and DRLSE.

Tables 3–8 show a numerical comparison of the ESM with the above initialization methods performed on 180 US images of malignant tumors, cysts, and fibroadenomas. Since FFS and CoD failed with 0% correctly segmented tumors, we do not show their results. The tables reveal that the ESM leads practically in every category, with 100% correctly initialized and 100% correctly segmented images. PIG and QAI show good results for fibroadenoma images, but can not resolve cysts and malignant tumors. In many cases a part of the QAI initial contour is outside tumor (Fig. 5(f) (g), (n), (o)). This leads to incorrect segmentations. PIG often provides good initializations. Up to 85% of PIG contours are inside the object. However, the method requires a tracing procedure to find the candidate contours. The procedure often wrongly includes a strong edge outside the tumor located close to the actual boundary. In this case,

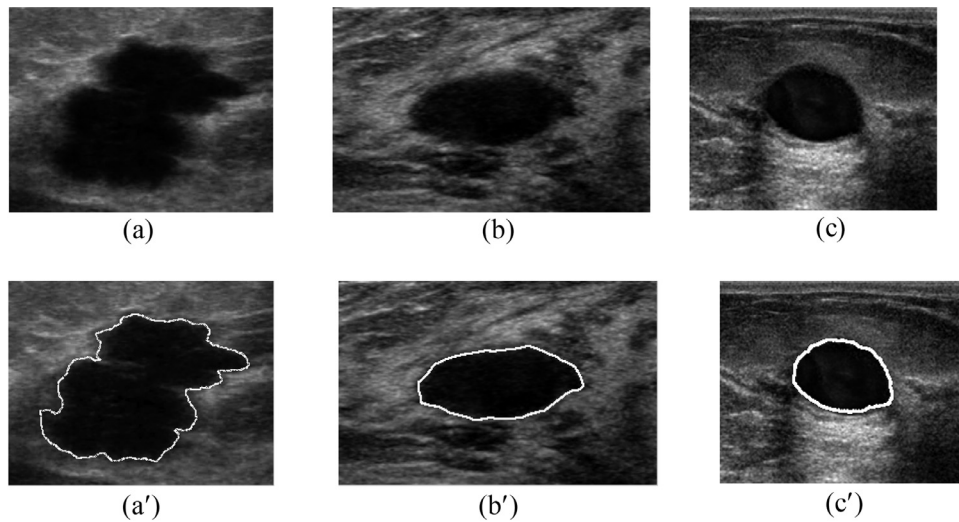


Fig. 4. Examples of the test images and their computerized segmentation: (a) malignant tumor (a') – segmentation, (b) fibroadenoma, (b')- segmentation, (c) cyst, (c')-segmentation.

Table 3
Comparison of the ESM with initialization methods for images of cysts, segmentation method- AC/ADF.

Model	Correctly initialized, $N_{corr}\%$	Correctly segmented, $S_{corr}\%$	Average accuracy							
			Contour-based measures				Region-based measures			
			H_1	H_2	H_3	TP_C	SEN	SPE	ACC	J
ESM/AC	100	100	5.46	2.59	2.57	92.78	97.07	99.61	99.20	0.99
QAI/AC	85	50	21.21	9.34	8.27	71.27	90.93	97.85	96.43	0.97
PIG/AC	65	80	15.76	5.74	5.23	80.14	84.45	97.94	86.55	0.97

Table 4
Comparison of the ESM with initialization methods for images of cysts, segmentation method-LSM/DRLSE.

Model	Correctly initialized, $N_{corr}\%$	Correctly segmented, $S_{corr}\%$	Average accuracy							
			Contour-based measures				Region-based measures			
			H_1	H_2	H_3	TP_C	SEN	SPE	ACC	J
ESM/LSM	100	100	5.18	2.05	1.85	93.81	97.06	99.65	99.23	0.99
QAI/LSM	85	70	16.23	3.65	3.30	68.45	96.22	96.74	97.08	0.96
PIG/LSM	65	65	21.77	8.06	7.18	65.35	78.86	95.91	91.30	0.90

Table 5
Comparison of the ESM with initialization methods, images for malignant tumors, segmentation method AC/ADF.

Model	Correctly initialized, $N_{corr}\%$	Correctly segmented, $S_{corr}\%$	Average accuracy							
			Contour-based measures				Region-based measures			
			H_1	H_2	H_3	TP_C	SEN	SPE	ACC	J
ESM/AC	100	100	6.24	0.96	1.10	91.89	97.19	98.79	98.33	0.97
QAI/AC	87	50	27.83	5.88	5.25	56.71	81.49	96.19	92.60	0.90
PIG/AC	73	53	23.20	5.35	4.97	67.07	91.50	95.84	95.05	0.93

the segmentation method can not move the contour further to the actual boundary (Fig. 5(h),(i), (p),(q)). Knowing that the seed is inside the tumor is a great advantage of ESM, leading to 100% correctly segmented images and a better segmentation accuracy.

For instance, in terms of $dist_{H_3}$, the average accuracy of the ESM/AC on malignant tumors is 1.1 pixels versus 5.25 for QAI and 4.97 for PIG. The ESM/LSM provides slightly better results-1.02 vs. 3.57 for QAI and 7.26 for PIG. Note that TS produces approximately the same initialization results as the ESM. However, the TS model is extremely slow. Our numerical experiments show that the ESM is approximately 10 times faster. Interestingly, the combination ESM/LSM always produces a better accuracy, as compared with the ESM/AC. As far as the different types of tumors are con-

cerned, ESM/LSM is the best for the malignant tumors in terms of $dist_{H_3}$ and the best for fibroadenomas, in terms of $dist_{H_2}$. However, the best region based accuracy ESM/LSM shows for the images of cysts. In summary, if we award one point for the best segmentation accuracy in each category, the absolute winner is ESM/LSM.

5. Conclusions

The proposed new automatic procedure for initialization of active contours for segmentation of ultrasound images of breast cancer outperforms preceding algorithms. In terms of the accuracy, the ESM is better than QAI, CoD, FFS, and PIG methods, and is comparable with TS. However, the particles are faster than TS. This is because TS may get stacked between the edges or inside the cav-

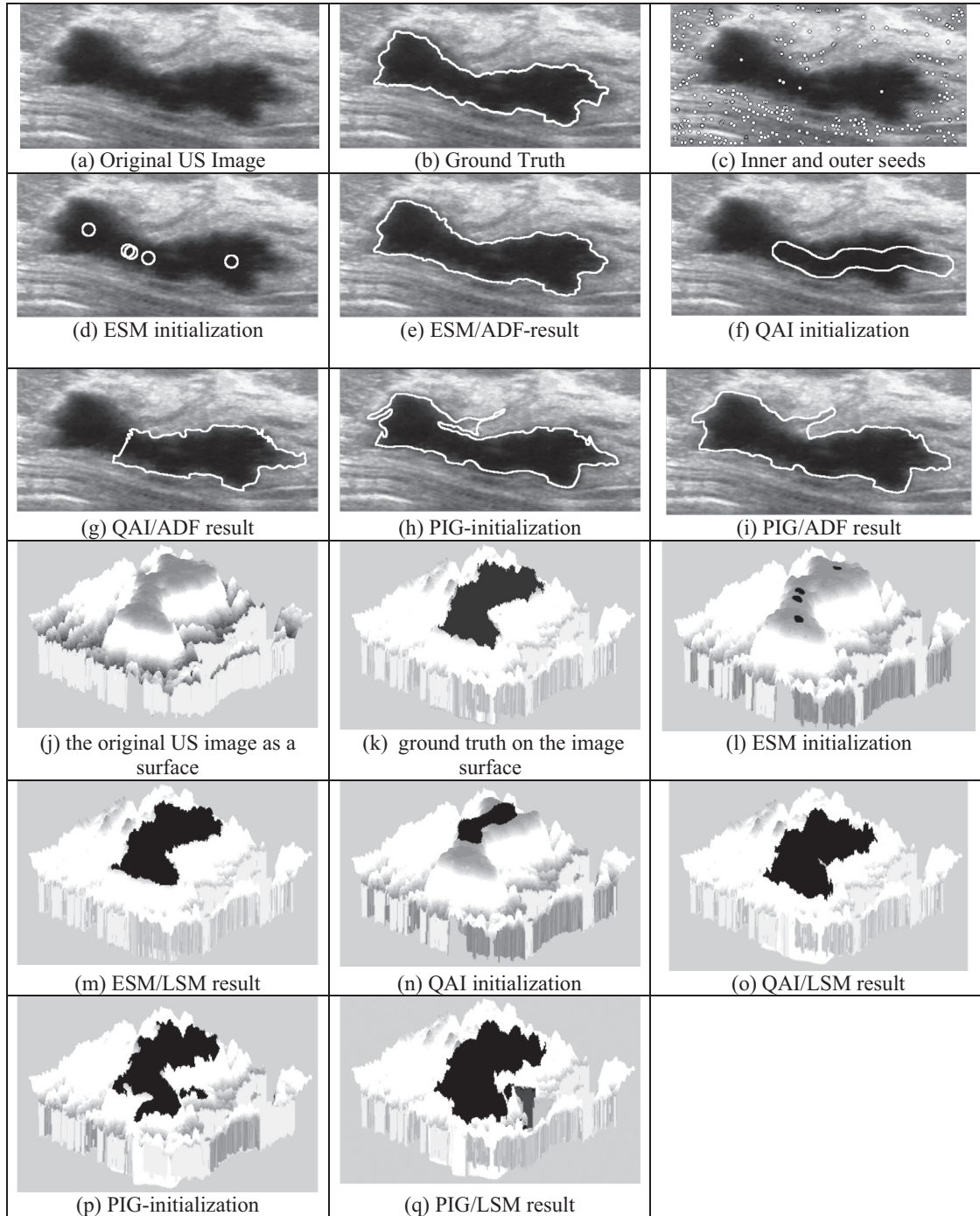


Fig. 5. (a)–(i) the initialization methods combined with the AC, (j)–(q) the initialization methods combined with the LSM.

Table 6
Comparison of the ESM with the initialization methods for images of malignant tumors, segmentation method- LSM/DRLSE.

Model	Correctly initialized, $N_{corr}\%$	Correctly segmented, $S_{corr}\%$	Average accuracy							
			Contour-based measures				Region-based measures			
			H_1	H_2	H_3	TP_C	SEN	SPE	ACC	J
ESM/LSM	100	100	5.56	0.90	1.02	91.95	96.64	98.96	98.34	0.97
QAI/LSM	87	80	17.45	3.30	3.57	67.98	94.45	96.52	96.43	0.95
PIG/LSM	73	50	26.52	7.39	7.26	53.05	93.11	93.67	93.85	0.91

Table 7

Comparison of the ESM with initialization methods for images of fibroadenoma, segmentation method- AC/ADF.

Model	Correctly initialized, $N_{\text{corr}}\%$	Correctly segmented, $S_{\text{corr}}\%$	Average accuracy							
			Contour-based measures				Region-based measures			
			H_1	H_2	H_3	TP_C	SEN	SPE	ACC	J
ESM/AC	100	100	5.13	1.32	1.92	92.81	98.27	98.56	98.80	0.99
QAI/AC	100	90	6.87	1.76	2.51	89.36	97.58	99.19	98.37	0.98
PIG/AC	80	80	15.40	4.59	4.23	78.71	87.42	97.37	96.13	0.94

Table 8

Comparison of the ESM with the initialization methods on images of fibroadenoma, segmentation method- LSM/DRLSE.

Model	Correctly initialized, $N_{\text{corr}}\%$	Correctly segmented, $S_{\text{corr}}\%$	Average accuracy							
			Contour-based measures				Region-based measures			
			H_1	H_2	H_3	TP_C	SEN	SPE	ACC	J
ESM/LSM	100	100	4.73	0.82	1.17	93.02	98.75	98.94	98.93	0.99
QAI/LSM	100	90	6.71	1.17	1.65	89.94	97.71	99.11	98.78	0.98
PIG/LSM	80	80	16.58	5.00	4.83	76.43	87.02	96.82	95.79	0.94

Table 9

Efficiency, the ESM vs. conventional methods.

Model	Initialization time	Correctly initialized $N_{\text{corr}}, \%$	Segmentation method	
			ADF/GGVF	LSM
ESM	fast (2–4 s)	excellent (100)	fast 1.25–2.0 s	fast 2.0–2.5 s
TS	very slow (60–90 s)	excellent (96.7)		
QAI	slow (15–23 s)	good (90.6)		
PIG	very fast (0.5–0.8 s)	medium (72)		
CoD	very fast (1–2 s)	very poor (0)		
FFS	very fast (1–2 s)	very poor (0)		

ities. As far as QAI, CoD, FFS, and PIG are concerned, their weakness is that they analyze the vector fields which can be irregular and chaotic. As opposed to that, the ESM uses the vector field only when it generates the seeds. Further, the algorithm is based on the edge map information. Table 9 presents a summary of the numerical experiments. The ESM is the fastest and the most accurate method. Although the LSM is slightly slower than ADF, the most suitable combination is ESM/LSM.

Acknowledgments

We wish to thank the anonymous Referees of the paper for valuable remarks. This research is sponsored by the [Thailand Research Fund](#), grant [BRG5780012](#), and the Center of Excellence in Biomedical Engineering, Thammasat University.

References

- [1] M. Kass, A. Witkin, D. Terzopoulos, Snakes: active contour models, *Intern. J. Comput. Vis.* 1 (4) (1988) 321–331.
- [2] C. Xu, J.L. Prince, Snakes, shapes, and gradient vector flow, *IEEE Trans. Image Process.* 7 (3) (1998) 359–369.
- [3] C. Xu, J.L. Prince, Generalized gradient vector flow external forces for active contours, *Signal Process* 71 (2) (1998) 131–139.
- [4] J. Tang, A multi-direction GVF snake for the segmentation of skin cancer images, *Pattern Recognit* 42 (6) (2009) 1172–1179.
- [5] M. Wei, Y. Zhou, M. Wan, A fast snake model based on non-linear diffusion for medical image segmentation, *Comput. Med. Imaging Graph.* 28 (3) (2004) 109–117.
- [6] N. Jifeng, W. Chengke, L. Shigang, Y. Shuqin, NGVF: an improved external force field for active contour model, *Pattern Recognit. Letters* 28 (1) (2007) 58–63.
- [7] L. Guillot, C.L. Guyader, Extrapolation of vector fields using the infinity Laplacian and with applications to image segmentation, *Scale Space Variational Methods Comput. Vis.* (2009) 87–99.
- [8] Y. Wang, Y. Jia, L. Liu, Harmonic gradient vector flow external force for snake model, *Electron. Lett.* 44 (2) (2008) 105–106.
- [9] B. Li, S.T. Acton, Active contour external force using vector field convolution for image segmentation, *IEEE Trans. Image Process.* 16 (8) (2007) 2096–2106.
- [10] J. Cheng, S.W. Foo, Dynamic directional gradient vector flow for snakes, *IEEE Trans. Image Process.* 15 (6) (2006) 1563–1571.
- [11] Y. Wu, Y. Wang, Y. Jia, Adaptive diffusion flow active contours for image segmentation, *Comput. Vis. Image Underst.* 117 (10) (2013) 1421–1435.
- [12] A. Rodtook, S.S. Makhnov, Multi-feature gradient vector flow snakes for adaptive segmentation of the ultrasound images of breast cancer, *J. Vis. Commun. Image Represent.* 24 (8) (2013) 1414–1430.
- [13] C. Li, J. Liu, M.D. Foxa, Segmentation of external force field for automatic initialization and splitting of snakes, *Pattern Recognit* 38 (11) (2005) 1947–1960.
- [14] Y. Wang, J. Liang, Y. Jia, On the critical point of gradient vector flow snake, *ACCV2007, LNCS 4844*, pp 754– (2007) 763.
- [15] G. Xingfei, T. Jie, An automatic active contour model for multiple objects, in: *Proc. Internat. Conf. Pattern Recognit.*, 2, 2002, pp. 881–884.
- [16] Y. He, Y. Luo, D. Hu, Semi-automatic initialization of gradient vector flow snakes, *J. Electron. Imag.* 15 (4) (2006) 1–8.
- [17] C.F. Shu, R.C. Jain, Vector field analysis for oriented patterns, *IEEE Trans. Pattern Anal. Mach. Intell.* 16 (9) (1994) 946–950.
- [18] I. Cohen, I. Herlin, A motion computation and interpretation framework for oceanographic satellite images, in: *Proc. Internat. Symposium Comput. Vis.*, Nov 1995, 1995, pp. 13–18.
- [19] J. Li, W.Y. Yau, H. Wang, Combining singular points and orientation image information for fingerprint classification, *Pattern Recognit* 41 (1) (2008) 353–366.
- [20] J. Li, W.Y. Yau, H. Wang, Constrained nonlinear models of fingerprint orientations with prediction, *Pattern Recognit* 39 (1) (2006) 102–114.
- [21] X. Tian, S. Samarasinghe, G. Murphy, An integrated algorithm for detecting position and size of knots on logs using texture analysis, in: *Proc. Conf. Image and Visions Computing*, 1999, pp. 121–132.
- [22] W.Y. Yau, J. Li, H. Wang, Nonlinear phase portrait modeling of fingerprint orientation, in: *Internat. Conf. Control, Automation, Robotics and Vision (ICARCV2004 8th)*, Dec 2004, 2004, pp. 1262–1267.
- [23] N. Ray, S.T. Acton, Merging parametric active contours within homogeneous image regions for MRI-based lung segmentation, *IEEE TMI* 22 (2) (2003) 189–199.
- [24] B.N. Saha, N. Ray, H. Zhang, Snake validation: A PCA-based outlier detection method, *IEEE Signal Process. Lett.* 16 (6) (2009) 549–552.
- [25] C. Tauber, H. Batatia, A. Ayache, Quasi-automatic initialization for parametric active contours, *Pattern Recognit. Lett.* 31 (1) (2010) 83–90.
- [26] C. Tauber, H. Batatia, A. Ayache, A general quasi-automatic initialization for Snakes: application to ultrasound images, in: *IEEE Internat. Conf. Image Processing*, 2, 2005, pp. 806–809.
- [27] B. Li, S.T. Acton, Automatic active model initialization via Poisson inverse gradient, *IEEE Trans. Image Process.* 17 (8) (2008) 1406–1420.
- [28] C.Y. Hsu, C.Y. Liu, C.M. Chen, Automatic segmentation of liver PET images, *Comput. Med. Imag. Graph.* 32 (7) (2008) 601–610.

- [29] C.Y. Hsua, H.F. Wang, H.C. Wang, K.K. Tseng, Automatic extraction of face contours in images and videos, *Future Gener. Comput. Syst.* 28 (1) (2012) 322–335.
- [30] E. Veronesea, R. Stramarec, A. Campiona, B. Raffainerb, V. Beltramec, E. Scagliori, A. Coranc, L. Cipriani, U. Fioccob, E. Grisana, Improved detection of synovial boundaries in ultrasound examination by using a cascade of active-contours, *Med. Eng. Phys.* 35 (2) (2013) 188–194.
- [31] D.J. Doshi, D.E. March, G.M. Crisi, B.F. Coughlin, Complex cystic breast masses: diagnostic approach and imaging-pathologic correlation, *Radiographics* 27 (2007) 53–64.
- [32] I.S. Jung, D. Thapa, G.N. Wang, Automatic segmentation and diagnosis of breast lesions using morphology method based on ultrasound, in: *Internat. Conf. on Fuzzy Systems and Knowledge Discovery (FSKD)*, August 2005, LNAI 3614, 2005, pp. 1079–1088.
- [33] A. Madabhushi, D.N. Metaxas, Combining low-, high-level and empirical domain knowledge for automated segmentation of ultrasonic breast lesions, *IEEE Trans. Med. Imag.* 22 (2) (2003) 155–169.
- [34] S. Selvan, S. Shenbagadevi, Automatic seed point selection in ultrasound echography images of breast using texture features, *Biocybernet. Biomed. Eng.* 35 (3) (2015) 157–168.
- [35] K. Fergani, D. Lui, C. Scharfenberger, A. Wong, D.A. Clausi, Hybrid structural and texture distinctiveness vector field convolution for region segmentation, *Comput. Vis. Image Underst.* 125 (2014) 85–96.
- [36] S. Liu, Y. Peng, A local region-based Chan–Vese model for image segmentation, *Pattern Recognit.* 45 (7) (2012) 2769–2779.
- [37] Y.S. Akgul, C. Kambhamettu, M. Stone, Extraction and tracking of the tongue surface from ultrasound image sequences, in: *Proc. Internat. IEEE Comput. Society Conf. Comput. Vis. and Pattern Recognit.*, 1998, pp. 298–303.
- [38] K. Kirimasthong, A. Rodtook, U. Chaumrattanakul, S.S. Makhanov, Phase portrait analysis for automatic initialization of multiple snakes for segmentation of the ultrasound images of breast cancer, *Pattern Anal. Applic.* 20 (1) (2017) 239–251.
- [39] A.C. Jalba, M.H.F. Wilkinson, J.B.T.M. Roerdink, Automatic Image Segmentation Using a Deformable Model Based on Charged Particles, in: *Lecture Notes in Computer Science*, 3211, 2004, pp. 1–8.
- [40] R. Rangayyan, F. Ayres, Gabor filters and phase portraits for the detection of architectural distortion in mammograms, *Med. Biol. Eng. Comput.* 44 (2006) 883–894.
- [41] D. Jordan, P. Smith, *Nonlinear Ordinary Differential Equations: An Introduction for Scientists and Engineers*, forth ed., Oxford University Press, Oxford, New York, 2007.
- [42] S. Chucherd, A. Rodtook, S.S. Makhanov, Phase portrait analysis for multiresolution generalized gradient vector flow, *IEICE Trans. Inf. & Syst.* E93-D (2010) 2822–2835.
- [43] M.-P. Dubuisson, A.K. Jain, A modified Hausdorff distance for object matching, in: *Proceedings. International Conference on Pattern Recognition, Israel*, 1994, 1994, pp. 566–568.
- [44] S. Osher, J.A. Sethian, Fronts propagating with curvature-dependent speed: algorithms based on Hamilton–Jacobi formulations, *J. Comput. Phys.* 79 (1998) 12–49.
- [45] V. Caselles, G.Sapiro R.Kimmel, A geometric model for active contours, *Int. J. Comput. Vis.* 22 (1) (1997) 61–79.
- [46] C. Li, C. Xu, C. Gui, M.D. Fox, Level set evolution without re-initialization: a new variational formulation, in: *Proceedings of IEEE Conference on Computer Vision and Pattern Recognition*, 2005, pp. 430–436.
- [47] C. Li, C. Xu, C. Gui, M.D. Fox, Distance regularized level set evolution and its application to image segmentation, *IEEE Trans. Image Process.* 19 (12) (2010) 3243–3254.
- [48] X. Yang, X. Gao, D. Tao, X. Li, Improving level set method for fast auroral oval segmentation, *IEEE Trans. Image Process.* 23 (7) (2014) 2854–2965.
- [49] D. Mumford, J. Shah, Optimal approximations by piecewise smooth functions and associated variational problems, *Commun. Pure Appl. Math.* 42 (5) (1989) 577–685.
- [50] T.F. Chan, L.A. Vese, Active contours without edges, *IEEE Trans. Image Process.* 10 (2) (2001) 266–277.
- [51] A. Tsai, A. Yezzi, A.S. Willsky, Curve evolution implementation of the Mumford–Shah functional for image segmentation, denosing, interpolation, and magnification, *IEEE Trans. Image Process.* 10 (8) (2001) 1169–1186.
- [52] T. Brox, D. Cremers, On the statistical interpretation of the piecewise smooth Mumford–Shah functional, in: *Proceedings of SSVM*, 2007, pp. 203–213.
- [53] C. Li, C. Kao, J.C. Gore, Z. Ding, Implicit active contours driven by local binary fitting energy, in: *Proceedings of IEEE Conference on Computer Vision and Pattern Recognition*, 2007, pp. 1–7.
- [54] C. Liu, W. Liu, W. Xing, An improved edge-based level set method combining local regional fitting information for noisy image segmentation, *Signal Proc* 130 (2017) 12–21.
- [55] W. Liu, Y. Shang, X. Yang, Active contour model driven by local histogram fitting energy, *Pattern Recognit. Lett.* 34 (2013) 655–662.
- [56] G. Gao, C. Wen, H. Wang, Fast and robust image segmentation with active contours and Student’s-t mixture model, *Pattern Recogn.* 63 (2017) 71–86.
- [57] H. Zhao, T. Chan, B. Merriman, S. Osher, A variational level set approach to multiphase motion, *J. Comput. Phys.* 127 (1) (1996) 179–195.
- [58] H. Ali, N. Badshah, K. Chen, G.A. Khan, A variational model with hybrid images data fitting energies for segmentation of images with intensity inhomogeneity, *Pattern Recognit.* 51 (2016) 27–42.
- [59] H. Min, X.-F. Wang, D.-S. Huang, W. Jia, A novel dual minimization based level set method for image segmentation, *Neurocomputing* 214 (2016) 910–926.
- [60] X.-F. Wang, H. Min, L. Zou, Y.-G. Zhang, A novel level set method for image segmentation by incorporating local statistical analysis and global similarity measurement, *Pattern Recognit.* 48 (2015) 189–204.
- [61] L. He, Z. Peng, B. Everding, X. Wang, C.Y. Han, K.L. Weiss, W.G. Wee, A comparative study of deformable contour methods on medical image segmentation, *Image and Vision Comp.* 26 (2008) 141–163.

Dr. Stanislav S. Makhanov received the M.Sc. degree in Applied Mathematics from the Moscow State University in 1981 and the Dr.Sc. from the Computing Center of the Russian Academy of Science in 1988, where he worked as an Associate Professor until 1993. From 1994 until 1999 he was a Visiting Professor with King Mongkut's Institute of Technology, Ladkrabang and Associated Faculty with the Asian Institute of Technology of Thailand. He is currently a Full Professor and a Head of a Center of Excellence in Biomedical Engineering with Sirindhorn International Institute of Technology, Thammasat University of Thailand. He is teaching courses in Applied Mathematics and Computer Science.